Sciencexpress Report

Complete Methods Set for Scalable Ion Trap Quantum Information Processing

J. P. Home,* D. Hanneke, J. D. Jost, J. M. Amini, D. Leibfried, D. J. Wineland

Time and Frequency Division, National Institute of Standards and Technology, Boulder, CO 80305, USA.

*To whom correspondence should be addressed. E-mail: jonathan.home@gmail.com

Large-scale quantum information processors must be able to transport and maintain quantum information, and repeatedly perform logical operations. Here we demonstrate a combination of all the fundamental elements required to perform scalable quantum computing using qubits stored in the internal states of trapped atomic ions. We quantify the repeatability of a multi-qubit operation, observing no loss of performance despite qubit transport over macroscopic distances. Key to these results is the use of different pairs of $^{9}Be^{+}$ hyperfine states for robust qubit storage, readout and gates, and simultaneous trapping of $^{24}Mg^{+}$ "re-cooling" ions along with the qubit ions.

The long term goal for experimental quantum information processing is to realize a device involving large numbers of qubits and even larger numbers of logical operations (*1*, *2*). These resource requirements are defined both by the algorithms themselves, and the need for quantum error-correction, which makes use of many physical systems to store each qubit (*1*, *3*). The required components for building such a device are robust qubit storage, single and two-qubit logic gates, state initialization, readout, and the ability to transfer quantum information between spatially separated locations in the processor (*2*, *4*, *5*). All of these components must be able to be performed repeatedly in order to realize a large scale device.

One experimental implementation of quantum information processing uses qubits stored in the internal states of trapped atomic ions. A universal set of quantum logic gates has been demonstrated using laser addressing (*6*–*8*), leading to a number of small-scale demonstrations of quantum information protocols including teleportation, dense-coding, and a single round of quantum error-correction (*6*). A major challenge for this implementation is now to integrate scalable techniques required for large-scale processing.

A possible architecture for a large-scale trapped-ion device involves moving quantum information around the processor by moving the ions themselves, where the transport is controlled by time varying potentials applied to electrodes in a multiple-zone trap array (*5*, *9*, *10*). The processor would consist of a large number of processing regions working in parallel, with other regions dedicated to qubit storage (memory). A general prescription for the required operations in a single processing region is the following (illustrated in Fig. 1), which includes all of the elements necessary for universal quantum computation (*11*). (i) Two qubit ions are held in separate zones, allowing individual addressing for single qubit gates, state readout, or state initialization. (ii) The ions are then combined in a single zone, and a two-qubit gate is performed. (iii) The ions are separated, and one is moved to another region of the trap array. (iv) A third ion is brought into this processing region from another part of the device. In this work we implement in a repeated fashion all of the steps which must be performed in a single processing region in order to realize this architecture.

Some elements of this architecture have been demonstrated in previous experiments (*6*, *12*), which involved transport of ions in a multi-zone trap. However, these experiments did not involve the use of techniques required for building a large scale device, limiting the size of algorithms which could be performed. Primary limiting factors for these experiments were the loss of qubit coherence, caused by interaction with the fluctuating magnetic field environment, and motional excitation, which degrades the fidelity of subsequent two-qubit gates because of the finite wavelength of the gate control fields (*13*). Motional excitation occurs as a result of imperfect control during transport and noisy electric fields emanating from the electrode surfaces (*6*). In this work, we store qubits robustly using a pair of energy eigenstates in the $^{9}Be^{+}$ $2s\ ^{2}S_{1/2}$ hyperfine manifold (shown in Fig. 2) whose energy separation does not depend on the magnetic field to first order. For the $^{9}Be^{+}$ "qubit" ions used here, this condition is met at a magnetic field of 0.011964 T for the "memory" qubit states $|1\rangle \equiv |F = 1, M_F = 0\rangle$ and $|0\rangle \equiv |F = 2, M_F = 1\rangle$ (The states are labeled using the total angular momentum quantum numbers F and M_F). The insensitivity to magnetic field changes is crucial for preserving coherence in the presence of ambient temporal field fluctuations (*14*), and also greatly suppresses phase shifts caused by spatial variations in the average field experienced by an ion as it is transported throughout the multi-zone trap array. We remove motional excitation prior to each two-qubit gate by recooling "refrigerant" $^{24}Mg^{+}$ ions that are trapped along with the qubit ions. Laser cooling this second species sympathetically cools

the first through the strong Coulomb interaction between the ions (*15–18*).

A benchmark for scalability in this implementation is the repeated performance of a complete set of one and two-qubit logic gates combined with quantum information transport. We demonstrate repeatability of a unitary transformation $\hat{U}$ which involves four single qubit gates, a two-qubit gate, and transport over 960 μm (the sequence for $\hat{U}$ is shown in Fig. 3a). Ideally, $\hat{U}$ implements the operation

$$\hat{U} = -\frac{e^{-i\pi/4}}{\sqrt{2}}\begin{pmatrix} -1 & 0 & 0 & i \\ 0 & 1 & i & 0 \\ 0 & i & 1 & 0 \\ i & 0 & 0 & -1 \end{pmatrix} \quad (1)$$

in the $|11\rangle$, $|10\rangle$, $|01\rangle$, $|00\rangle$ basis. We directly compare experimental implementation of $\hat{U}$ and $\hat{U}^2$ using quantum process tomography (*19*). Process tomography requires the process under investigation to be applied to sixteen input states, followed by measurement in nine orthogonal bases (*20*). The input states are prepared using a combination of optical pumping and single-qubit operations, with the latter performed on each qubit individually. The analysis also requires individual single-qubit rotations, followed by individual state measurement of the qubits. The experiment therefore realizes all of the basic components illustrated in Fig. 1. We directly compare $\hat{U}$ and $\hat{U}^2$ by running the experimental sequence for a given input/output combination on $\hat{U}$ and $\hat{U}^2$ sequentially (shown in Fig. 3b), making the comparison of the two robust against long term drifts in experimental parameters. For each input/analysis combination, we repeat this sequence 350 times.

The experiment utilizes two $^9Be^+$ and two $^{24}Mg^+$ ions, trapped in a six-zone linear Paul trap (*12*). Each $^9Be^+$ ion is used to store one qubit, and is accompanied at all times by a $^{24}Mg^+$ refrigerant ion, which is used for sympathetic cooling. The ion order is initialized to $^9Be^+$ -$^{24}Mg^+$ -$^{24}Mg^+$ -$^9Be^+$ at the start of the experimental sequence, and remains in this order throughout (*21*).

Coherent manipulations of the internal and motional states of the ions are performed using laser-induced stimulated Raman transitions (*9*). Single qubit gates are implemented in the basis $|1\rangle$, $|0\rangle$ by resonant Rabi flopping, applying the rotation

$$R(\theta,\varphi) = \begin{pmatrix} \cos(\theta/2) & -ie^{-i\varphi}\sin(\theta/2) \\ -ie^{i\varphi}\sin(\theta/2) & \cos(\theta/2) \end{pmatrix} \quad (2)$$

where θ is proportional to the Raman pulse duration and ϕ is chosen by adjusting the relative phase of the Raman light fields at the ion. We individually address the two qubit ions by holding them in two trap zones 240 μm apart, and switching the laser beams between zones.

To implement two-qubit gates, we first combine all of the ions into a single zone. The four-ion linear chain exhibits four axial vibrational normal modes caused by the Coulomb coupling between ions (*21*). After recombination, these modes contain significant excess energy, mainly caused by imperfect control of the potentials used during separation and recombination. Therefore, prior to each two-qubit gate, we cool each mode to near the quantum ground state ($\langle n\rangle \sim 0.06$) using a combination of Doppler cooling and resolved sideband cooling on the $^{24}Mg^+$ ions (*15*, *22*). Importantly, the cooling light only interacts with $^{24}Mg^+$, leaving the qubits stored in $^9Be^+$ intact (*15*).

The composite two-qubit gate makes use of a geometric phase gate (*7*) to implement $\hat{G} = D[(1, i, i, 1)]$, where $D[\underline{v}]$ is a diagonal matrix with the vector $\underline{v}$ on the diagonal. The phase acquired by the $|10\rangle$ and $|01\rangle$ states is obtained by transient simultaneous excitation of the two highest-frequency normal modes by use of a state-dependent optical dipole force (*22*). The state dependence of this force is derived from a differential light shift between the two qubit states, which is highly suppressed for field-independent transitions (*14*, *23*). We thus use a hybrid scheme for qubit storage, mapping the qubits into a different state manifold for the two-qubit gate (*22, 24*, *25*). Prior to applying the optical dipole force, we transfer each qubit into a pair of states with a sizeable differential light shift - the "gate" manifold $|1_G\rangle \equiv |1,1\rangle$, $|0_G\rangle \equiv |2,2\rangle$ (Fig. 2). After applying the state-dependent force, we reverse this transfer and the ions are again separated (*22*). The gate manifold is sensitive to magnetic field fluctuations, which can lead to qubit dephasing. We suppress these effects using spin-echo techniques (*21*).

We employ quantum process tomography to characterize our implementation of the unitary operation $\hat{U}$, including any experimental imperfections (*19*, *20*). The evolution of the qubit system (including that caused by undesired interactions with the environment) is described by a completely positive linear map $\rho_{out} = E_{\hat{U}}(\rho_{in})$ (*19*) on the input density matrix $\rho_{in} = \sum_{i,j} c_{i,j} |i\rangle\langle j|$, where the $c_{i,j}$ are complex numbers and i, j are labels that each run over the eigenstates $|11\rangle$, $|10\rangle$, $|01\rangle$, $|00\rangle$. Following (*26*), we represent the map by a 16 × 16 matrix

$$E_{\hat{U}} = \sum_{i,j} |i\rangle\langle j| \otimes E_{\hat{U}}(|i\rangle\langle j|) \quad (3)$$

In order to extract this process matrix, we experimentally apply the process to 16 input states made up of tensor products of the states $|1\rangle$, $|0\rangle$, $(|0\rangle - |1\rangle)/\sqrt{2}$ and $(|0\rangle + i|1\rangle)/\sqrt{2}$. For each output density matrix, we apply nine sets of rotations, which allow us to measure the expectation values of the operators $\sigma_s \otimes \sigma_t$, where the $\sigma_{s,t}$ run over the Pauli matrices I, σ_x, σ_y, σ_z. Our state readout performs a projective

measurement in the Z basis on each ion independently. We first transfer population from $|0\rangle$ to $|2,2\rangle$, and from $|1\rangle$ to $|1,-1\rangle$, and subsequently drive the cycling transition $2s\ ^2S_{1/2}$ $|2,2\rangle \leftrightarrow 2p\ ^2P_{3/2}\ |3,3\rangle$ for 200 μs, where $|2,2\rangle$ strongly fluoresces and $|1,-1\rangle$ does not (*22*). We collect a small fraction of the emitted photons on a photomultiplier tube. We run the sequence shown in Fig. 3b 350 times for each of the 16 input states and nine measurement rotations. The process matrix is obtained directly from the recorded photon counts and measurement/preparation settings using a maximum-likelihood method that ensures that the reconstructed process matrix is physical (*26*).

Experimentally obtained process matrices for one and two applications of $\hat{U}$ are shown in Fig. 4. From the reconstructions, we can calculate various measures of the fidelity with which the processes were implemented. A direct comparison between experimental results and the ideal case is given by the entanglement fidelity $F \equiv \mathrm{Tr}(E_{\mathrm{ideal}}\, E)/16$ (*27*). We find $F_{\hat{U}} = 0.922(4)$ for a single application of $\hat{U}$, and $F_{\hat{U}^2} = 0.853(5)$ for two applications (error estimates are the standard error on the mean obtained from parametric bootstrap resampling (*22*)). As an additional measure of operation fidelity, we take the mean $\overline{f}$ of the fidelity

$$f(\rho_{\mathrm{ideal}}, \rho_E) \equiv \left[\mathrm{Tr}\left(\sqrt{\sqrt{\rho_{\mathrm{ideal}}}\, \rho_E \sqrt{\rho_{\mathrm{ideal}}}} \right) \right]^2 \quad (28)$$

between the output density matrices obtained from the ideal and experimental processes for an unbiased set of 36 input states (formed from the eigenstates of $\sigma_s \otimes \sigma_t$, where $\sigma_{s,t}$ run over $\sigma_x, \sigma_y, \sigma_z$). We obtain a mean state fidelity of $\overline{f}_{\hat{U}} = 0.940(4)$ for $E_{\hat{U}}$ and $\overline{f}_{\hat{U}^2} = 0.890(4)$ for $E_{\hat{U}^2}$. We can compare these values to the entanglement fidelities using the relation $\overline{f} = (4F + 1)/5$ (*27*), and see that they are consistent.

To compare the performance of a second application of $\hat{U}$ relative to the first, we can compare its experimental repetition $E_{\hat{U}^2}(\rho_{\mathrm{in}})$ to a numeric repetition of the experimental map $E_{\hat{U}}(\rho_{\mathrm{in}})$, i.e., to $E_{\hat{U}\hat{U}}(\rho_{\mathrm{in}}) \equiv E_{\hat{U}}(E_{\hat{U}}(\rho_{\mathrm{in}}))$. Evaluating the fidelities for each against the ideal case yields $F_{\hat{U}^2}/F_{\hat{U}\hat{U}} = 1.003(13)$ and $\overline{f}_{\hat{U}^2}/\overline{f}_{\hat{U}\hat{U}} = 1.004(10)$, indicating that the operation fidelity is the same for each application of $\hat{U}$. We can also make a direct comparison between the processes performed by our implementation of $\hat{U}$ and $\hat{U}^2$ by taking the mean fidelity between $\rho_{\hat{U}\hat{U}} = E_{\hat{U}}(\hat{U}(\rho_{\mathrm{in}}))$ and $\rho_{\hat{U}^2} = E_{\hat{U}^2}(\rho_{\mathrm{in}})$ for the 36 input states. We find $\overline{f}(\rho_{\hat{U}\hat{U}}, \rho_{\hat{U}^2}) = 0.987(3)$. Although this number is not unity, as might be expected, the deviation can be ascribed to bias in the maximum-likelihood reconstruction method for finite sample size (*22*). Our results are thus consistent with the same operation being performed by the experiment for each application of $\hat{U}$.

Sources of error in our system arise primarily from spontaneous photon scattering (~ 1.5% per $\hat{U}$) (*29*) and intensity fluctuations of the Raman light fields at the percent level. In order to characterize the loss of fidelity caused by single-qubit rotations, we apply process tomography to the experimental sequence, but without the state-dependent force pulses. In this case the ions are always in a product state and the process matrix for each can be obtained independently. The resulting process matrices have mean state fidelity relative to the ideal case of 0.97 for a single run of the sequence (which uses eight rotations per ion including qubit manifold transfer and spin-echo pulses). During the two-qubit gate, the spin states are entangled with the motion. From separate measurements of motional coherence, we estimate the infidelity from this source to be less than 1×10^{-3}.

Many challenges remain before large-scale ion trap quantum information processing becomes a reality, including increasing fidelities to those required for fault-tolerant quantum error correction (*3*, *1*), and meeting the considerable technical challenge of controlling ions in large multi-dimensional trap arrays (*10*). Both of these challenges could potentially contain problems which have not been considered here, and which may require combining our approach with alternative methods, for instance entanglement distribution using photonic networks (*30*). Nevertheless, the combination of techniques demonstrated here includes all of the basic building blocks required in this architecture, and opens up new possibilities for quantum information processing as well as state and process engineering.

References and Notes

1. E. Knill, *Nature* **434**, 39 (2005).
2. A. M. Steane, *Quant. Inf. Comp.* **7**, 171 (2007).
3. A. M. Steane, *Phys. Rev. A* **68**, 042322 (2003).
4. D. P. DiVincenzo, *Fortschr. Phys.* **48**, 771 (2000).
5. D. Kielpinski, C. Monroe, D. J. Wineland, *Nature* **417**, 709 (2002).
6. R. Blatt, D. J. Wineland, *Nature* **453**, 1008 (2008).
7. D. Leibfried *et al*., *Nature* **422**, 412 (2003).
8. J. Benhelm, G. Kirchmair, C. F. Roos, R. Blatt, *Nat. Phys.* **4**, 463 (2008).
9. D. J. Wineland *et al*., *J. Res. Natl. Inst. Stand. Technol.* **103**, 259 (1998).
10. R. B. Blakestad *et al*., *Phys. Rev. Lett.* **102**, 153002 (2009).
11. A. Barenco *et al*., *Phys. Rev. A* **52**, 3457 (1995).
12. M. D. Barrett *et al*., *Nature* **429**, 737 (2004).
13. A. Sørensen, K. Mølmer, *Phys. Rev. A* **62**, 022311 (2000).
14. C. Langer *et al*., *Phys. Rev. Lett.* **95**, 060502 (2005).
15. M. D. Barrett *et al*., *Phys. Rev. A* **68**, 042302 (2003).
16. H. Rohde *et al*., *B: Quantum Semiclass. Opt.* **3**, S34 (2001).
17. B. B. Blinov *et al*., *Phys. Rev. A* **65**, 040304 (2002).
18. J. P. Home *et al*., *Phys. Rev. A* **79**, 050305 (2009).

19. M. A. Nielsen, I. L. Chuang, *Quantum Computation and Quantum Information* (Cambridge University Press, Cambridge, 2000).
20. M. Riebe *et al*., *Phys. Rev. Lett.* **97**, 220407 (2006).
21. J. D. Jost *et al*., *Nature* **459**, 683 (2009).
22. Material and methods are available as supporting material on *Science* Online.
23. P. J. Lee *et al*., *B: Quantum Semiclass. Opt.* **7**, S371 (2005).
24. N. Lundblad, J. M. Obrecht, I. B. Spielman, J. V. Porto, *arXiv:0902.3213* (2009).
25. G. Kirchmair *et al*., *Phys. Rev. A* **79**, 020304 (2009).
26. Z. Hradil, J. Rehácek, J. Fiurásek, M. Jezek, *Quantum State Estimation* (Springer-Verlag, 2004), chap. Maximum-Likelihood Methods in Quantum Mechanics, pp. 59-112.
27. M. Horodecki, P. Horodecki, R. Horodecki, *Phys. Rev. A* **60**, 1888 (1999).
28. R. Jozsa, *J. Mod. Opt.* **41**, 2315 (1994).
29. R. Ozeri *et al*., *Phys. Rev. A* **75**, 042329 (2007).
30. D. L. Moehring *et al*., *Nature* **449**, 68 (2007).
31. This work was supported by IARPA and the NIST Quantum Information Program. J. P. H. acknowledges support from a Lindemann Trust Fellowship. We thank E. Knill for helpful discussions, J. J. Bollinger for technical assistance and Y. Colombe for comments on the manuscript. This paper is a contribution by the National Institute of Standards and Technology and not subject to U.S. copyright.

Supporting Online Material
www.sciencemag.org/cgi/content/full/1177077/DC1
Materials and Methods
References

1 June 2009; accepted 8 July 2009
Published online 6 August 2009; 10.1126/science.1177077
Include this information when citing this paper

Fig. 1. Schematic of the sequence of operations implemented in a single processing region for building up a computation in the architecture of (*9*, *5*). A large-scale device would involve many of these processing regions performing operations in parallel, along with additional regions for memory. Generalized operations would use this block structure repeatedly, with perhaps some of the steps omitted.

Fig. 2. Hybrid qubit storage in the $^{9}Be^{+}$ 2s $^{2}S_{1/2}$ hyperfine levels. The states are labeled using the total angular momentum quantum numbers F and M_F. $|1\rangle$, $|0\rangle$ are the qubit states used for single qubit gates and transport, and $|1_G\rangle$, $|0_G\rangle$ are used for two-qubit gates. For detection, the $|1,-1\rangle$ and $|2,2\rangle$ states are used. At the applied magnetic field ($B \cong$ 0.011964 T), the frequencies for transitions between pairs of states with the same F are well resolved.

Fig. 3. (**A**) Schematic of the qubit ion trajectories (solid red and dotted blue lines) and gate operations used to implement $\hat{U}$. The single qubit rotations are "$\pi/2$" $\equiv R(\pi/2, 0)$ (Eq. 2). The two-qubit gate implements $\hat{G} = D[(1,i,i,1)]$. (**B**) Full sequence used to perform process tomography on $\hat{U}$ and $\hat{U}^2$. This sequence is repeated 350 times for each setting of preparation/analysis.

Fig. 4. Reconstructed process matrix for (**A**) $\hat{U}$ and (**B**) two repetitions of $\hat{U}$. The map $E(|i\rangle\langle j|)$ produces a matrix $E_{k,l}$ for each element $|i\rangle\langle j|$. Hence elements of the matrix E are labeled by $m = 4(i-1) + k$, $n = 4(j-1) + l$, where the factor 4 results from the size of the two-qubit state space. For example, the $|11\rangle\langle 00|$ ($i = 1$, $j = 4$) element of an input density matrix is mapped to $E(|11\rangle\langle 00|)$, a 4×4 block of E given by $m \in [1, 4]$ and $n \in [13, 16]$. The position of each peak is in agreement with the theoretical prediction.

1) Individually addressed single-qubit gates, state readout, and state initialization

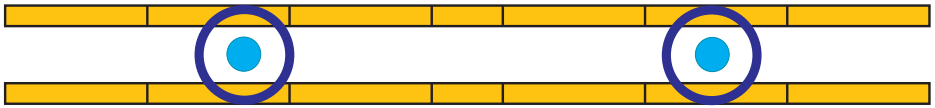

2) Two-qubit gate - qubit ions in single trap zone

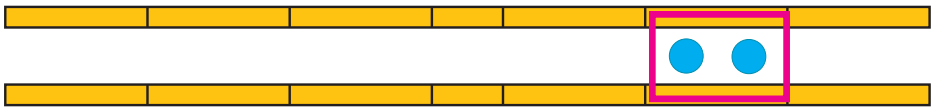

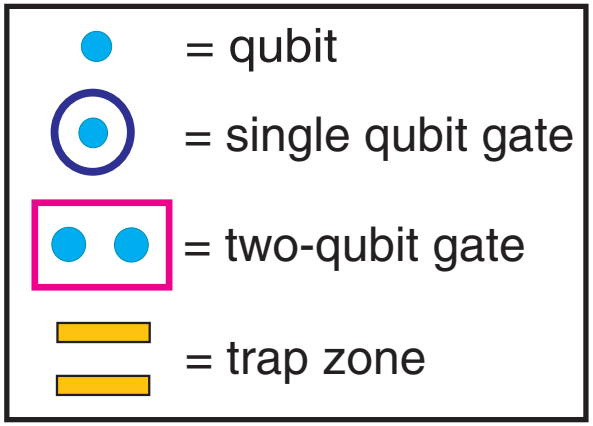

3) Transport - qubit ion 2 moved to another region of trap array

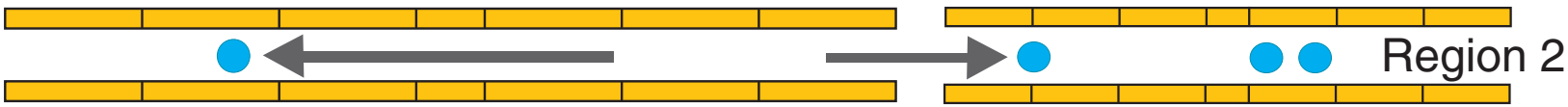

4) Transport - qubit ion 3 brought from a third region of the trap array

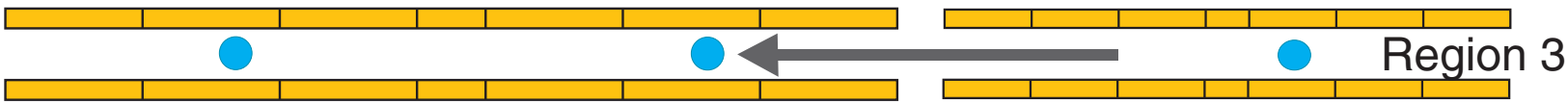

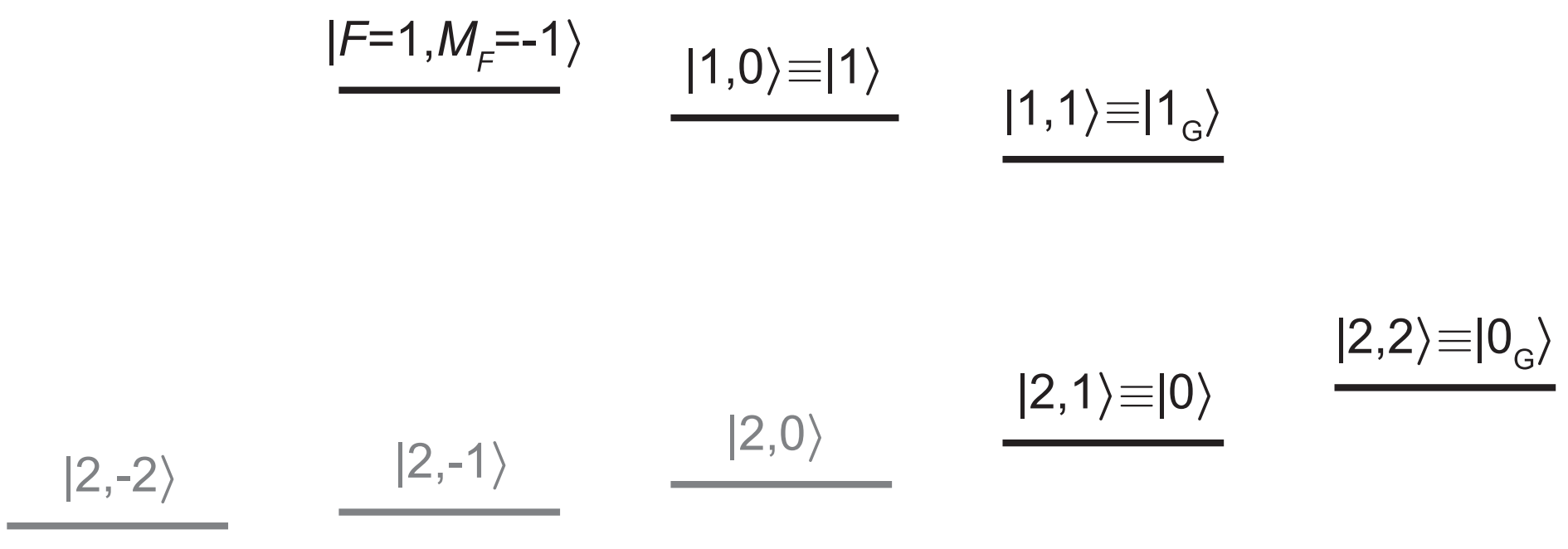
|F=1,M_F=-1⟩
|1,0⟩≡|1⟩
|1,1⟩≡|1_G⟩
|2,2⟩≡|0_G⟩
|2,1⟩≡|0⟩
|2,0⟩
|2,-1⟩
|2,-2⟩

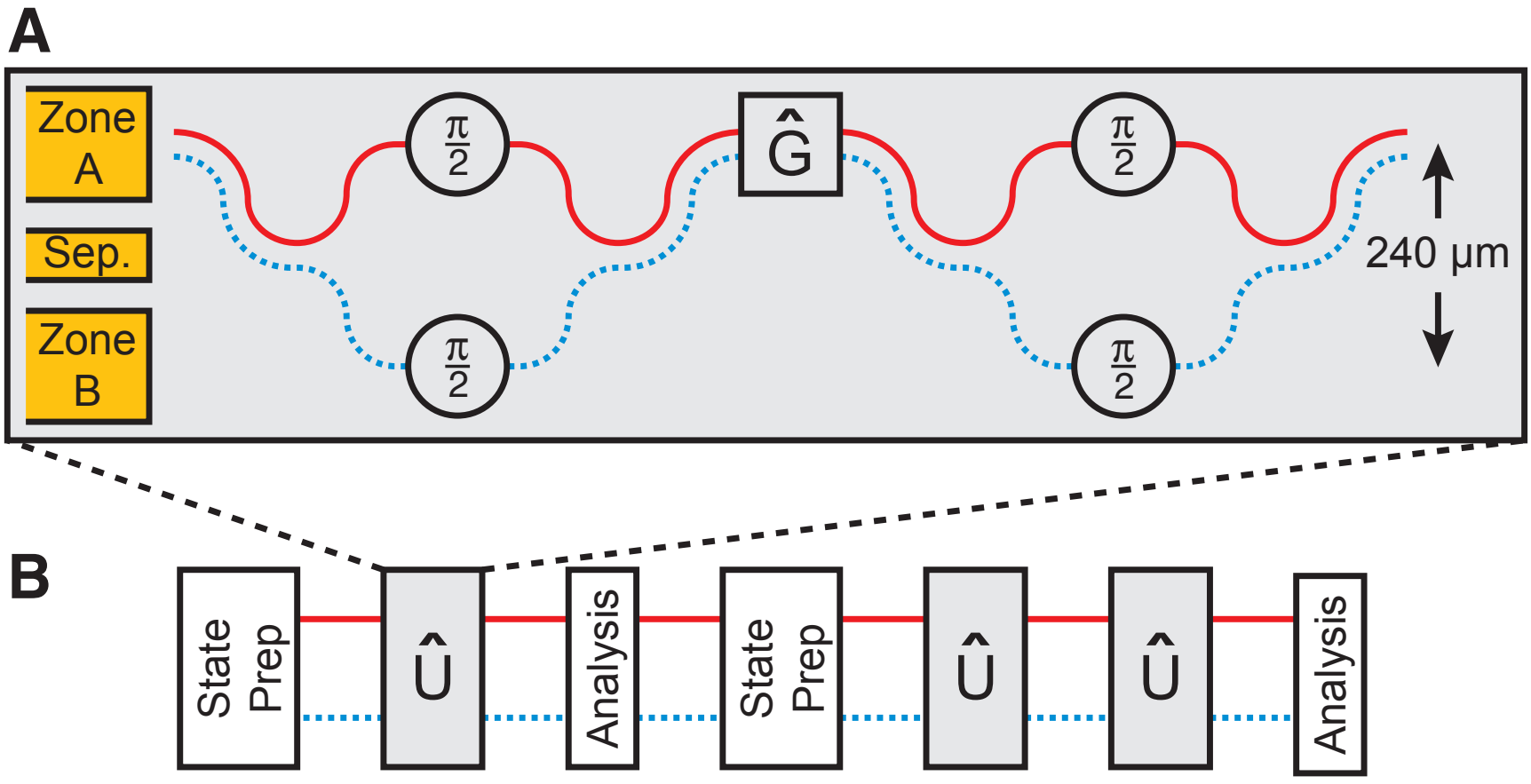
A
Zone A
Sep.
Zone B
π/2
Ĝ
π/2
π/2
π/2
240 μm
B
State Prep
Û
Analysis
State Prep
Û
Û
Analysis

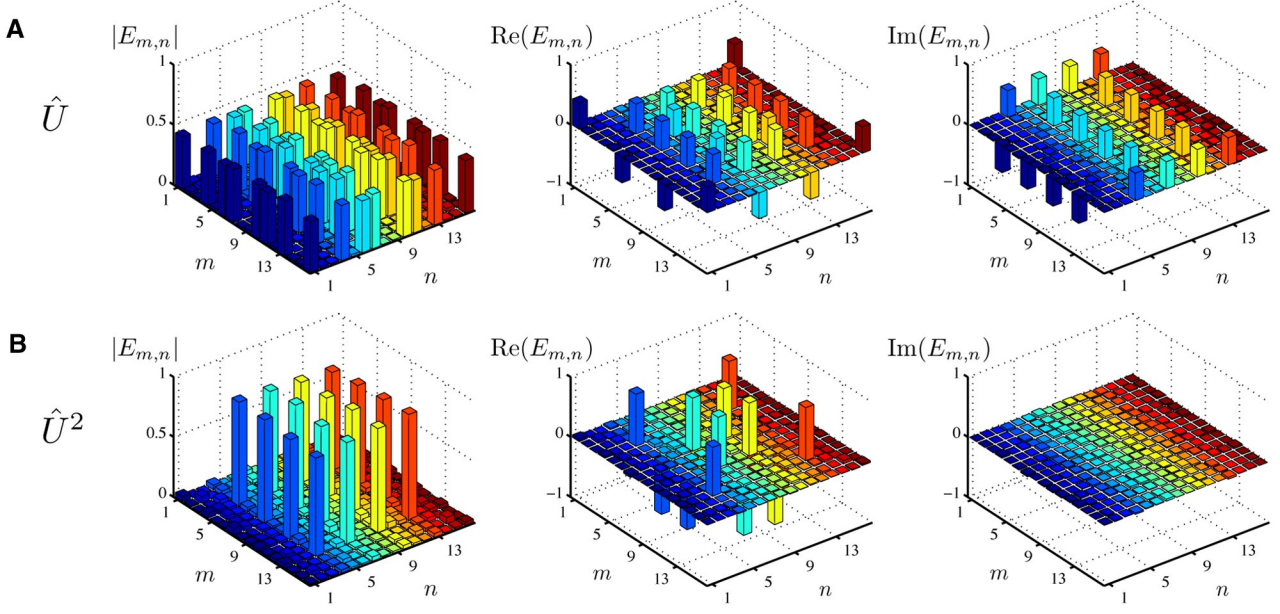
A
$\hat{U}$
$|E_{m,n}|$
$\mathrm{Re}(E_{m,n})$
$\mathrm{Im}(E_{m,n})$
B
$\hat{U}^2$
$|E_{m,n}|$
$\mathrm{Re}(E_{m,n})$
$\mathrm{Im}(E_{m,n})$
m
n